CHAPTER 5

H_2O_2 production on Ag/s-(Co_3O_4/$NiFe_2O_4$) visible light magnetically recyclable photocatalyst and its in-situ use for Fenton reaction

5.1 INTRODUCTION

There are four main issues in photocatalyst design. These are efficient photoexcitation of electrons and holes using visible light, valence band (VB), and conduction band (CB) positions, preventing recombination by charge separation and reactant adsorption to the photocatalyst surface. Semiconductor heterojunctions have structural options that can be manipulated to overcome these obstacles [176]. Such heterojunctions typically consist of a reduction and an oxidation component. The CB and the VB positions on these components should be such that it is thermodynamically feasible for them to reduce or oxidize the targeted species. The reactant to be reduced should properly adsorb on the reduction part, and the species to be oxidized should have an affinity toward the oxidation component [22,177].

The H_2O_2 production on a heterojunction photocatalyst requires oxygen reduction (on the reduction component of the heterostructure) and water oxidation ($2H_2O + h^+ \rightarrow O_2 + 4H^+ + 4e^-$) on the oxidation part of the composite photocatalyst [9,178]. Since UV radiation decomposes H_2O_2, it should be avoided in its photocatalytic production [179]**.** The heterojunction photocatalyst design strategies listed above can improve the H_2O_2 production rate significantly. Many studies have used noble metals (Au, Ag, Pt) based composite photocatalysts for H_2O_2 evolution due to their effective charge carrier separation, plasmonic behavior, and direct $2e^-$ oxygen reduction [36,180]**.** Meng et al. have reported H_2O_2 formation on Au and Ag-loaded graphitic carbon nitride (Au/g-C_3N_4 and Ag/g-C_3N_4) photocatalysts under visible light irradiation. Loading the g-C_3N_4 surface with noble metal nanostructures remarkably enhanced H_2O_2 formation because of the direct $2e^-$ oxygen reduction over the Au and Ag [181].

Another issue hampering the practical use of photocatalysts is the technology and cost of catalyst separation and reuse after each cycle. Non-magnetic nanoparticle-based photocatalysts are difficult to separate and reuse further, enhancing the cost of the photocatalyst. Fine non-magnetic nanoparticles could also be a source of secondary pollution. The development of magnetically recyclable photocatalysts can overcome these problems [182,183]. Superparamagnetic nanoparticles can be easily separated from the treated aqueous solution using an external magnet and re-dispersed using normal bath sonication. Recently, Pal et al. reported magnetically recyclable Ag/starch-Fe_3O_4/Ag_2O visible light photocatalysts for photocatalytic H_2O_2 production. This p-n heterojunction photocatalyst produced 2.16 mmol (millimoles) H_2O_2 in only one hour [59].

Investigators frequently face a problem while planning or designing a heterojunction photocatalyst for H_2O_2 production: which semiconductor component is more appropriate for oxygen adsorption, and which one prefers interaction with water. Large-scale classical molecular dynamics (MD) simulations can compute the same for the few oxygen molecules in an aqueous medium. Given the preceding discussion, the research presented in this paper is on the preparation of Ag-loaded starch functionalized Co_3O_4/$NiFe_2O_4$ heterojunction photocatalyst for H_2O_2 production. The latter was then in situ used for tetracycline degradation. The Ag/s-Co_3O_4/$NiFe_2O_4$ (starch functionalized is abbreviated as s-Co_3O_4/$NiFe_2O_4$) heterojunction photocatalysts have not been reported so far in the literature.

We used large-scale classical MD simulations to determine the relatively higher affinity of Co_3O_4 towards oxygen in water. Note that silver is a well-known material for 2e-O_2 reduction [48,59], which is required for efficient H_2O_2 formation. Then $NiFe_2O_4$ was selected as the magnetic semiconductor component because its bandgap was staggered compared to Co_3O_4. Starch stabilization of the composite improves its hydrophilicity,

which is necessary for better water oxidation. We designed and prepared Ag/s-Co_3O_4/$NiFe_2O_4$ heterojunction photocatalysts based on this information by hydrothermal and step-wise precipitation techniques. The prepared samples were characterized by XRD, TEM, and XPS techniques. The component bandgaps, band positions, and recombination issues were investigated by UV-visible diffuse reflectance spectroscopy (UV-DRS), Mott-Schottky, and photoluminescence studies on the as-prepared samples. A combination of experimental and computational results revealed the probable photocatalysis mechanism.

5.2 EXPERIMENTAL SECTION

5.2.1 Synthesis of bare Co_3O_4

Pure Co_3O_4 was synthesized by the following one-step hydrothermal method. Appropriate volumes of 0.1M of $Co(Ac)_2.4H_2O$ and 0.2M urea were dissolved in 50 mL of deionized double-distilled water (DDDW) and stirred for 60 min. Ammonia was added dropwise to this solution till pH 9 was reached, and then stirred for two more hours. The resulting reaction mixture was transferred to a 100 mL autoclave and kept at 180 ºC for 24 hours. The obtained precipitate was washed repeatedly with DDDW and finally with ethanol. Finally, it was dried at 60 ºC overnight and calcined at 400 ºC for 3 hours [184].

5.2.2 Synthesis of bare $NiFe_2O_4$

Initially, Ni $(NO_3)_2{\cdot}6H_2O$ (3.15 mmol) and Fe $(NO_3)_2{\cdot}2H_2O$ (6.3 mmol) were dissolved in 70 mL of DW. The mixture was continuously stirred for 3 hours. Then, an appropriate volume of 2M NaOH solution was added to bring the pH value of the reaction mixture to 13. Next, the reaction mixture was heated at 80 °C for one hour under vigorous stirring. The precipitate formed was centrifuged, rinsed ten times with distilled water (DW)/ethanol, and dried at 60 °C for 24 hours. The dried powder was calcined at 400 °C for 3 hours [86].

5.2.3 Synthesis of Co_3O_4/$NiFe_2O_4$ heterostructure photocatalyst

The above-prepared Co_3O_4 (300mg) powder was re-dispersed in 40 mL DDDW by bath sonication treatment for 1 hour. Equal volumes of 0.025M of $Ni(NO_3)_2.6H_2O$ and 0.050M of Fe $(NO_3)_2.9H_2O$ aqueous solution were mixed in 50 mL DW (1:2 ratio). This salt solution was then added to the re-dispersed suspension of Co_3O_4 nanoparticles. In the next step, the dropwise addition of a certain volume of 1M NaOH brought this reaction mixture to pH 13. The whole reaction mixture was heated at 80 ºC under stirring on a hot plate for one hour. The product formed was centrifuged and washed with DDDW and ethanol several times. The sample was dried at 60 ºC for 24 hours. After drying, it was further calcined at 400 ºC for three hours. The abbreviation CoNi denotes this nanocomposite sample in the rest of the paper.

5.2.4 Synthesis of Ag/s-Co_3O_4/$NiFe_2O_4$ photocatalyst

A specific amount of CoNi nanocomposite was dispersed in 30ml distilled water under bath sonication for 2 hours. After that, two Ag/s-Co_3O_4/$NiFe_2O_4$ nanocomposites were prepared using different amounts of the (10 and 20 weight% %) $AgNO_3$ precursor in the preparation protocol. These mixtures were shaken for 24 hours in a thermostatic agitator. Next, the mixture was heated at 60 °C, and suitable volumes of one-weight percent starch and glucose solutions were added to the above mixture under continuous stirring by a mechanical stirrer. Starch stabilization of the composite surfaces makes them more hydrophilic and stable against aggregation. The suspension pH was maintained at 8, and stirring continued for another hour at 60 °C. Next, the prepared sample was isolated by magnetic decantation, washed several times with DDDW/ethanol, and dried at 50°C [185]. In the rest of the paper, the finally obtained 10wt% Ag/s-Co_3O_4/$NiFe_2O_4$ is abbreviated

as10Ag/s-CoNi and 20wt%Ag/s-Co_3O_4/ $NiFe_2O_4$ as 20Ag/s-CoNi. Scheme 5.1 shows the synthesis pathway of Ag/s-(Co_3O_4/$NiFe_2O_4$) formation.

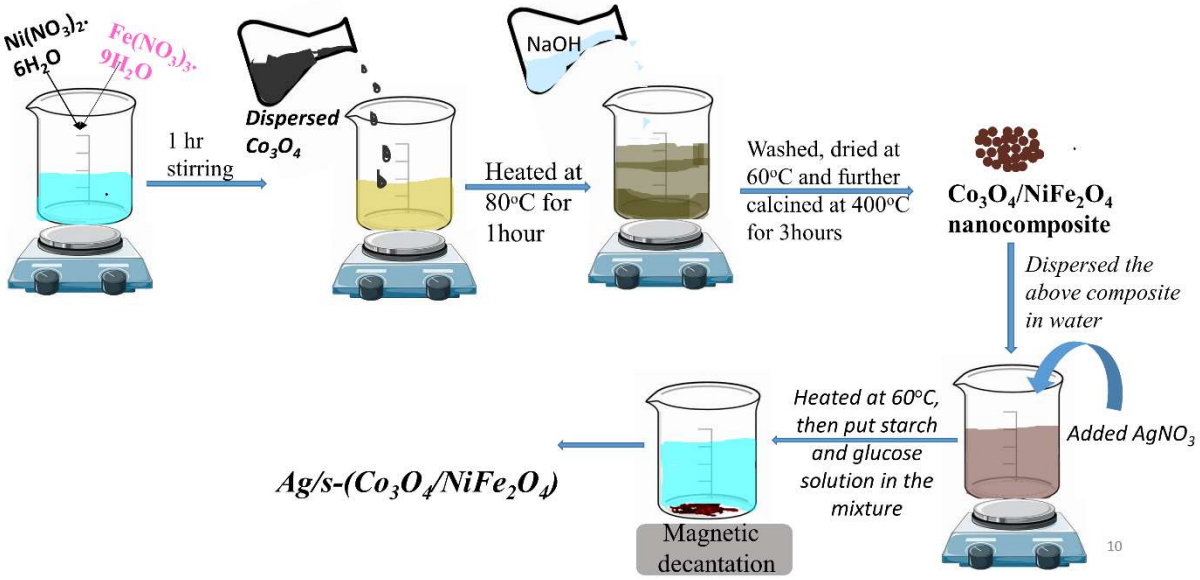

Scheme 5.1 Schematic representation synthesis pathway of Ag/s-(Co_3O_4/$NiFe_2O_4$) formation.

5.2.5 Photocatalytic H_2O_2 production activity

The following protocol was used to determine the photocatalytically produced H_2O_2 on the prepared nanocomposites. In this experiment, a 2 mg photocatalyst was added to 5 mL of distilled water and subjected to bath sonication for 10 min. Then, 600µL of this suspension was mixed with 5ml distilled water and allowed to stand in the dark for 1 hour. This suspension was placed in the photocatalytic reaction chamber and irradiated with the cool white LED (1070 W/meter^2) light. The temperature inside the photocatalytic chamber was 25°C throughout the visible light irradiation period. After one hour of irradiation, the sample was recovered by magnetic separation, and the H_2O_2 produced was determined by the standard $KMnO_4$ titration method [59]. The photocatalytic H_2O_2 produced was also

monitored under different pH conditions. The pH of the reaction mixture was changed by adding different volumes of 0.1M HCl. The optimum amount of H_2O_2 was formed at pH 3. Therefore, different control experiments were carried out at this pH. The control setups included carrying out this experiment with continuous purging of O_2 gas. Another control experiment used 5 mL of acetonitrile as the reaction medium with O_2 purging. The photocatalytic experiment was also carried out in a 4% isopropyl alcohol (IPA) aqueous solution with and without O_2 purging.

5.2.6 In-situ photo-Fenton tetracycline degradation

The objective of this experiment was to determine the in situ activity of the photocatalytically produced H_2O_2 towards photo-Fenton degradation of tetracycline. A series of experiments were carried out for this purpose. First, a 2 mg photocatalyst was added to 5 mL of distilled water and subjected to bath ultrasonication for 10 min. Then, 600µL of the re-dispersed photocatalyst was mixed with 5 mL of 10-ppm tetracycline solution. The reaction mixture pH was adjusted to 3 and allowed to stand in the dark for 40 minutes. Then, the reaction mixture was exposed to a cool white LED light. The temperature of the reaction chamber was 25 °C throughout the reaction. The photocatalytic degradation of tetracycline was analyzed by recording UV-visible spectra of the reaction mixture at regular time intervals. This photocatalytic experiment was also repeated with scavenger molecules specific to $OH\cdot$, $\cdot O_2^-$, and h^+ reactive species. Isopropanol (IPA), p-benzoquinone (PBQ), and potassium iodide (KI) were the scavengers for trapping the $OH\cdot$, $\cdot O_2^-$, and h^+ active species, respectively [186,187]. In the active species determination experiment, 150 µL (0.185 mM) of PBQ, KI, and IPA each were added to the reaction mixture. The rest of the experimental procedure remained the same. Thus, KI is used as a

hole scavenger, and PBQ is used to consume $O_{2^{\cdot}}^{-}$ radical and IPA to trap the $OH^{\cdot}$ radicals. Equation (5.1) below was used to calculate the degradation rate of the organic pollutant.

$$Percentage\ degradation\ tetracycline\ (D) = \left(\frac{C_o - C_t}{C_t}\right) \times 100 \quad \text{..... (5.1)}$$

Here, C_o and C_t denote the initial and final concentrations of tetracycline pollutants.

5.2.7 Model building and MD simulation

The Materials and Process Simulation (MAPS 4.01 Scienomics LLC) software was used to build the initial molecular model. Supercells of Co_3O_4 (dimensions: 25.20 Å x 33.60 Å x 8.40 Å) and $NiFe_2O_4$ (dimensions: 25.44 Å x 33.92 Å x 8.48 Å) were constructed from unit cells of Co_3O_4 (mp-18748) and the unit cell of $NiFe_2O_4$ (mp-22684), respectively. These supercells were cleaved using the surface builder tool (MAPS 4.01 software) to reveal the Co_3O_4 and $NiFe_2O_4$ slabs with (311) plane surfaces. A rectangular simulation box (dimensions: 35.97Å x 34.96 Å x 64 Å) was made using the interface builder plugin in MAPS software. The (311) plane of $NiFe_2O_4$ (slab depth 7 Å) made the top, while the Co_3O_4 slab (depth 7 Å) occupied the bottom of the cell. There was a 50Å interlayer distance between the above two slabs. Figure 5.1a displays the initial empty simulation cell. The initial water and oxygen molecule models were built using the MAPS molecule builder plugin. The TIP3P water model was used in this simulation. The space between the $NiFe_2O_4$ (top slab) and Co_3O_4 (bottom slab) was filled with 2000 H_2O and 20 O_2 molecules (Figure 5.1b). The overall density of the liquid phase in the interlayer space was ~1.01 g/cc. This simulation cell was then optimized using the conjugate gradient geometry optimization method. The Dreiding force field modeled the interactions between the atoms, making the adsorbent surface, water, and the oxygen molecules. These systems were then subjected to NVT ensemble MD simulations using the LAMMPS (Large-scale Atomic/Molecular

Massively Parallel Simulator) program. Periodic boundary conditions were employed on the three dimensions of all model systems. The temperature was fixed at T = 298.15 K in all simulations. The NVT ensemble MD simulation runs were 10 nanoseconds long with a time step of 1 fs. The data generated in the last 4 nanoseconds was used as the production run. Columbic interactions were calculated with the particle mesh approach using a cut-off distance of 12 Å.

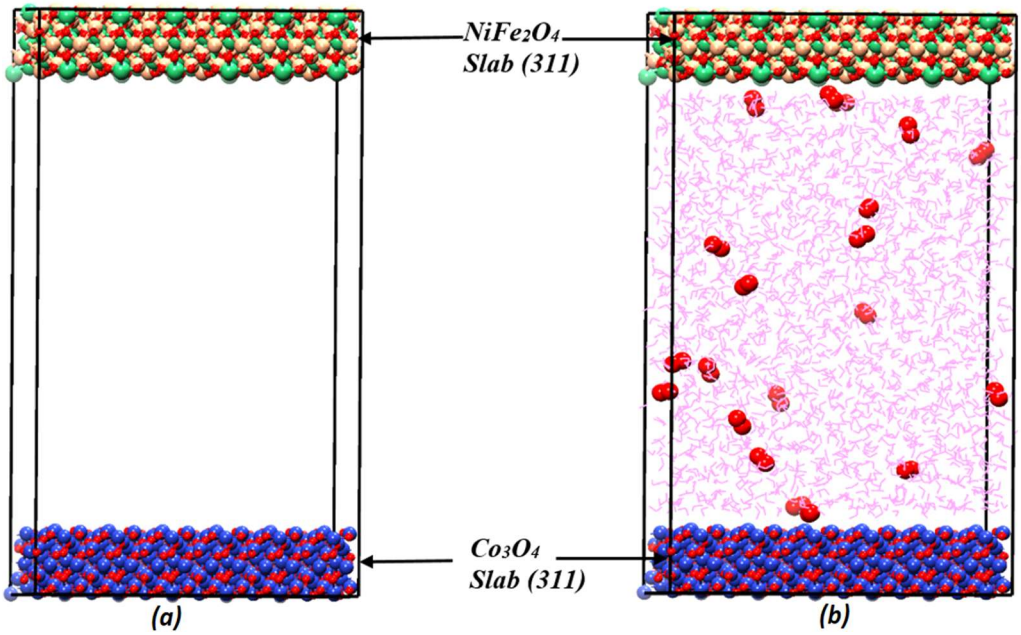

Figure 5.1 (a) Snapshot of an empty rectangular simulation cell with Co_3O_4 and $NiFe_2O_4$ slabs making up its two ends. **(b)** A snapshot of the initial configuration of the initial simulation cell after the insertion of 20 O_2 and 2000 water molecules [color scheme: Red-Oxygen, Pink- water, Purple- Hydrogen, Green- Nickel (Ni), Orange- Iron (Fe), and Blue-Cobalt (Co)].

5.3 RESULTS AND DISCUSSION

Figure 5.2 displays the XRD patterns of $NiFe_2O_4$, Co_3O_4, CoNi, 10Ag/s-CoNi, and 20Ag/s-CoNi samples. The XRD plots of Co_3O_4 and $NiFe_2O_4$ pure phases matched the cubic phases of $NiFe_2O_4$ (JCPDS No. #894927) and Co_3O_4 (JCPDS No. #761802). The

XRD plot of the nanocomposite CoNi displays only peaks identified with the cubic Co_3O_4 (JCPDS No. 761802) phase. There were no $NiFe_2O_4$ cubic phase peaks in this XRD. As we show later while presenting the TEM results, this is due to the extremely fine $NiFe_2O_4$ nanostructures (~6nm) formed in the CoNi composite. Such fine nanostructures result in broadened and very low-intensity XRD peaks, which are difficult to identify compared to the higher-intensity peaks of the other components in the composite. Both XRD plots of 10Ag/s-CoNi and 20Ag/s-CoNi samples display a prominent FCC Ag peak at 38.16 degrees, confirming the presence of Ag in the CoNi composite. The other peaks in the 10Ag/s-CoNi and 20Ag/s-CoNi samples were the same as the CoNi composite.

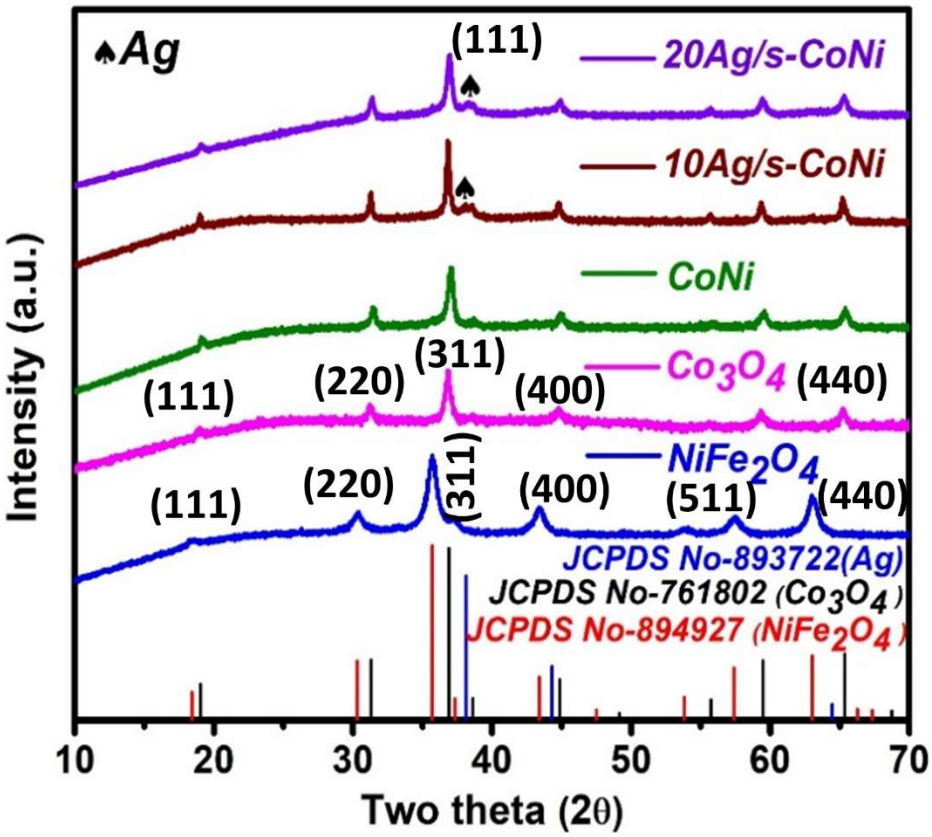

Figure 5.2 XRD spectra of $NiFe_2O_4$, Co_3O_4, CoNi, 10Ag/s-CoNi and 20Ag/s-CoNi composite

The morphology of $NiFe_2O_4$, Co_3O_4, and their composite nanoparticles was analyzed by HR-TEM. Figure 5.3a (TEM image) shows that the $NiFe_2O_4$ nanostructures

were spherical primarily, while Co_3O_4 particles in Figure 5.3b were found to have polyhedron shapes. Figure 5.3c displays nanoparticles of $NiFe_2O_4$ embedded on the Co_3O_4 nanostructures. The $NiFe_2O_4$ nanostructures on the Co_3O_4 surface were in the ~6 nm range. The HR-TEM image in Figure 5.3c and the calculated lattice fringes from Inverse Fast Fourier Transform (IFFT) in Figure 5.3e reveal two distinct types of lattice fringes with interplanar spacings of 0.476 nm and 0.25 nm, observed adjacent to each other. The former spacing corresponds to the (111) plane of Co_3O_4, while the latter is characteristic of the (311) plane of $NiFe_2O_4$, indicating the precipitation of $NiFe_2O_4$ on Co_3O_4 (as shown in Figures 5.3d and 5.3e). Figure 5.3f shows an image of a 10Ag/s-CoNi composite. Fig. 5.3g displays the HR-TEM of a region of this image. Three types of fringes spacing corresponding to Ag, Co_3O_4, and $NiFe_2O_4$ planes can be seen in this figure. The adjacent location of the FCC Ag fringe confirms the successful loading of Ag nanostructures over the CoNi sample.

Analysis of many nanocomposite structures using the Image J software showed that the Co_3O_4 nanostructures have a ~100 nm mean particle size. The $NiFe_2O_4$ nanostructures loaded on the bigger Co_3O_4 particles are much finer (average particle size ~6 nm). The much larger Co_3O_4 particle in the nanocomposite implies that there could be more Ag nanostructures loaded on the Co_3O_4 surface (Figure 5.3f). Figure 5.3h and 5.3i shows the Low resolution of TEM images elemental mapping of the 10Ag/s-CoNi photocatalyst. The mapping image of a typical 10Ag/s-CoNi nanocomposite particle shows that Ag is mainly on the Co_3O_4 part of the CoNi composite.

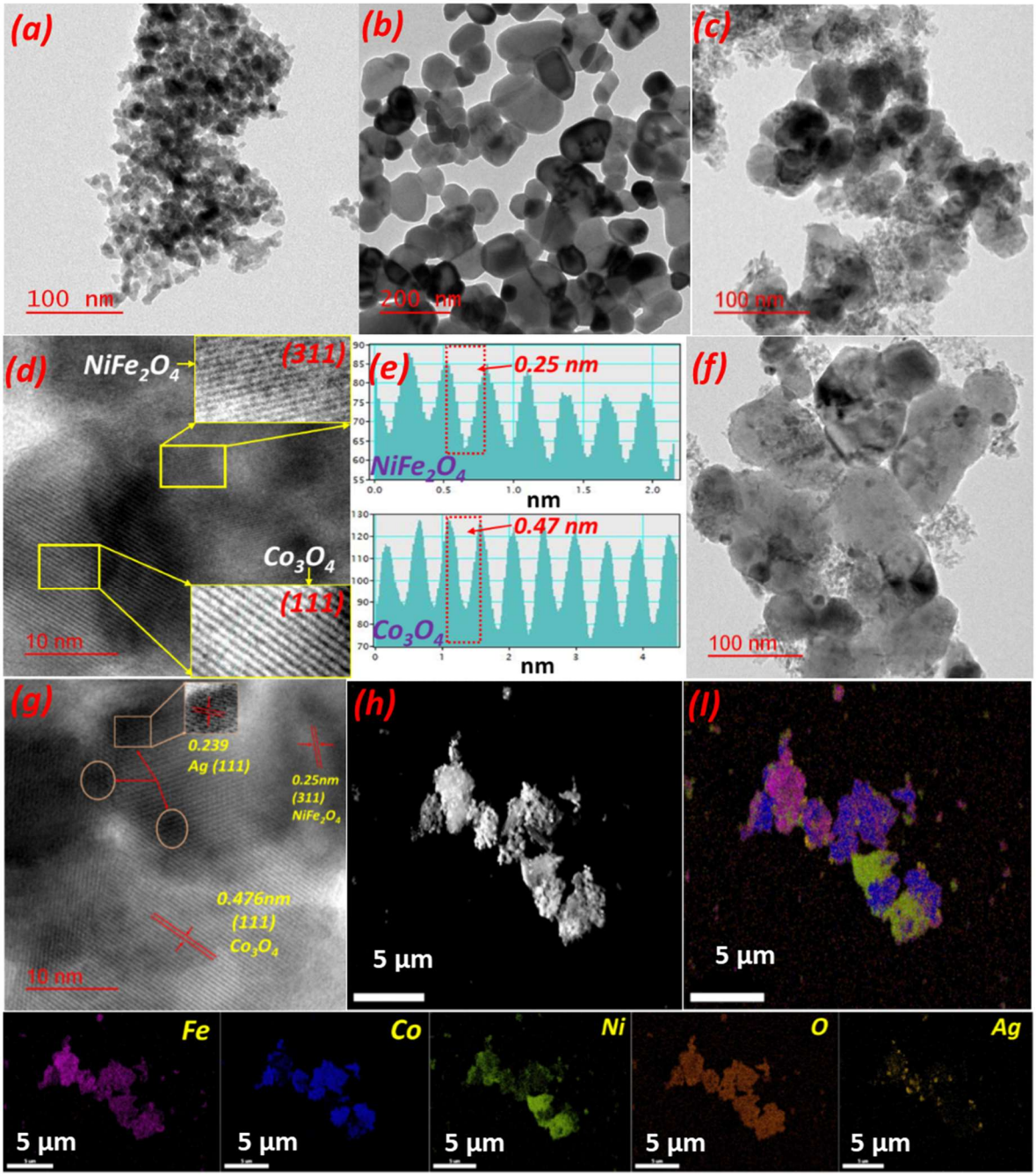

Figure 5.3 (a, b) represents the TEM image of pure $NiFe_2O_4$ and Co_3O_4 **(c, d)** TEM and HR-TEM of CoNi photocatalyst **(e)** IFFT analysis of CoNi sample **(f, g)** TEM and HR-TEM images of 10Ag/s-CoNi photocatalyst **(h, i)** Low-resolution TEM images and corresponding elemental mapping of 10Ag/s-CoNi sample.

The UV-visible DRS spectroscopy of the solid powders of the as-prepared photocatalysts was conducted to investigate their optical properties and band gaps. The

solid-state absorbance data for all the prepared photocatalysts are presented in Figure 5.4a. The Tauc equation, in combination with the Kubelka-Munk function, was applied to calculate the band gaps of the pure Co_3O_4 and $NiFe_2O_4$ photocatalysts (Figures 5.4 b, c) [188]. The x-axis intercepts of the linear fit of these plots indicate that the band gaps (Eg) of $NiFe_2O_4$ and Co_3O_4 are 1.97 eV and 2.15 eV, respectively.

To confirm the semiconductor type and band edge potential, a Mott-Schottky (MS) analysis was performed. Figures 5.4d, 5.4e, and 5.4f show the MS plots for pure Co_3O_4, $NiFe_2O_4$, and the CoNi composite materials. The experimental details of these electrochemical analyses are provided in Chapter 2 of this thesis. The MS analysis was conducted for all three samples at a consistent frequency of 1000 Hz. The MS plot of Co_3O_4 displays a linear plot with a negative slope, while the $NiFe_2O_4$ plot has a positive slope. The positive slope of $1/C^2$ versus V plots indicates that the photocatalyst is n-type, and the negative slope of the plot indicates that the semiconductor is p-type [100,157,189,190]. Figure 5.4f shows the MS plot of the CoNi composite. This plot shows one positive and one negative slope. A composite material having both negative and positive slope portions confirms that a p-n heterojunction has been formed [191]. The x-axis intercept of the linear fit to the positive slope portion gives the CB position of the n-type semiconductor. Similarly, the x-axis intercept of the linear fit to the negative slope portion is the VB position of the composite. The calculated band edges are shown in Fig. 5.4 (d-f). Furthermore, the Mott-Schottky data combined with the optical bandgap also gave us the band structure of the heterojunction photocatalyst. These characterization studies confirmed the formation of type II staggered heterojunction photocatalysts.

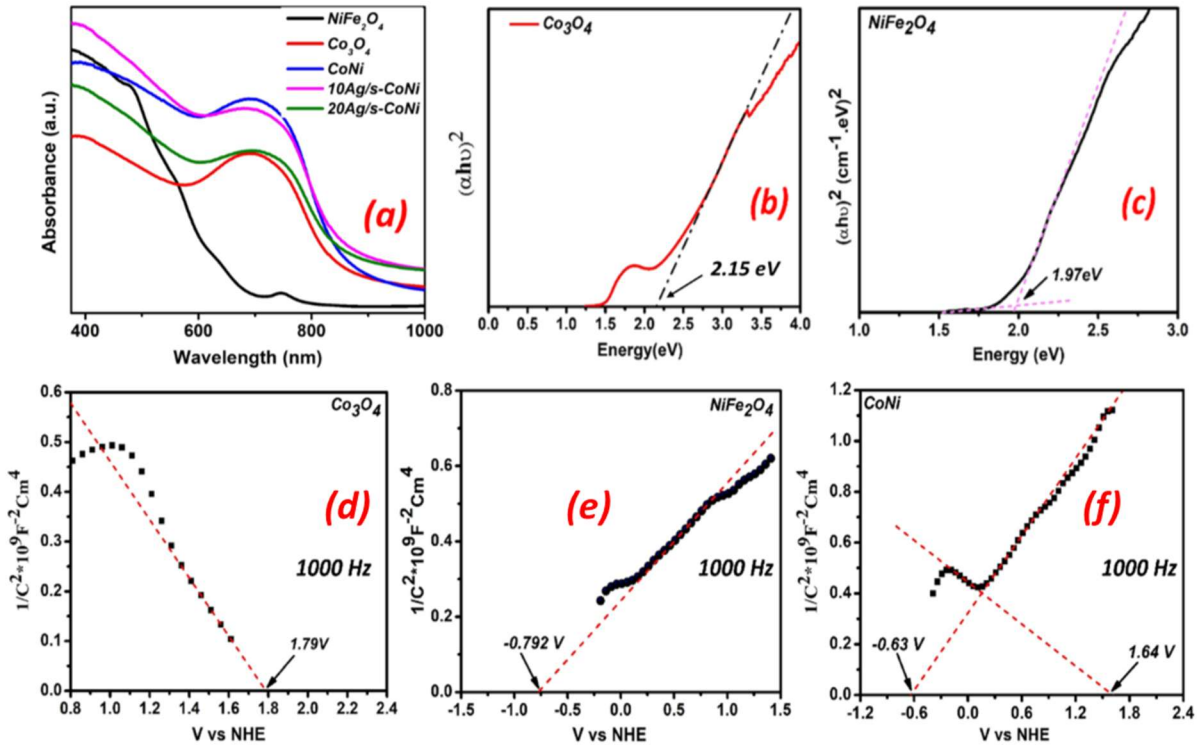

Figure 5.4 (a) UV absorbance spectra of all prepared photocatalysts **(b, c),** Tauc plot of Co_3O_4 and $NiFe_2O_4$**.** Mott-Schottky plot of **(d)** Co_3O_4**, (e)** $NiFe_2O_4$, **(f)** CoNi composite.

The composition, oxidation states, and electronic environment of the pure Co_3O_4, $NiFe_2O_4$, and 10Ag/s-CoNi composite were investigated using XPS. Figure 5.5a shows the high-resolution spectrum of the pure Co_3O_4 sample. The XPS of Co 2p spectra in Figure 5.5a shows Co $2p_{3/2}$ peaks at 778.8 eV and 780.2 eV and Co $2p_{1/2}$ peaks at 794.3 eV and 795.9 eV binding energies [192]. On formation of the 10Ag/s-CoNi composite, the Co $2p_{3/2}$ peaks in the Co 2p high-resolution XPS spectrum (Figure 5.5b) shifted to 779.3 and 780.9 eV. Fig. 5.5c displays three peaks Ni 2p (of $NiFe_2O_4$ nanoparticles) at binding energies 854.5, 855.8, and 872.4 eV that shift to 854.6, 856, and 872.9 eV (Figure 5.5d) in the XPS of the 10Ag/s-CoNi composite. Figure 5.5e shows the Fe 2p peaks at 710.2, 712.3, and 724.5 eV in the XPS of pure $NiFe_2O_4$ particles [160]. These increased to 710.5, 712.6, and 724.8 eV binding energies in the XPS of the 10Ag/s-CoNi composite. The O 1s peak is deconvoluted into regions with peaks at 529.6, 530.1, 531.3, 532.2, and 532.6 eV. The first

two peaks correspond to the lattice oxygen (M-O bonds), and the peak at 531.3 eV could be ascribed to hydroxyls and some defect sites [193,194]. The other two peaks, located at 532.2 and 532.6 eV, are recognized as chemically and physically adsorbed oxygen (Figure 5.5g) [195,196]. Furthermore, the Ag 3d XPS displays the two main peaks of Ag $3d_{3/2}$ and Ag $3d_{5/2}$ at 374 eV and 368 eV, respectively, due to Ag nanostructures in the 10Ag/s-CoNi composite (Figure 5.5h). Overall, Ag loading led to a positive shift in Co 2p, Ni 2p, and Fe 2p peaks. Such a shift implies the transfer of electrons from the Co_3O_4 and the $NiFe_2O_4$ phases to the Ag nanostructures.

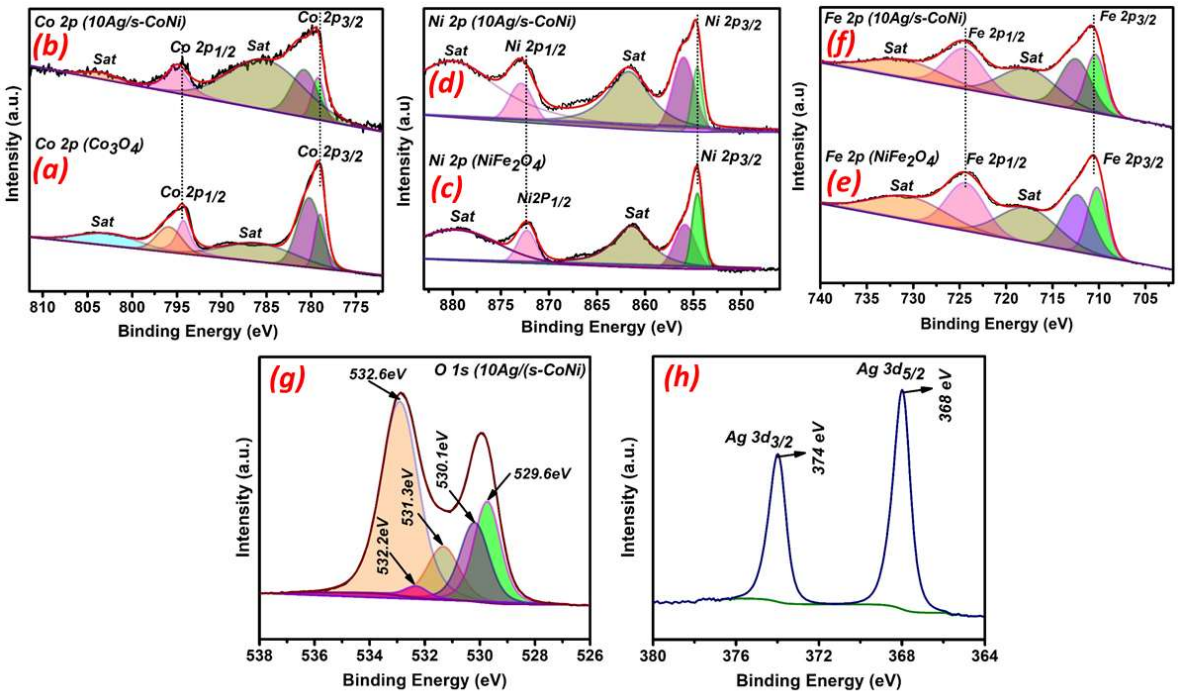

Figure 5.5. XPS analysis of the as-prepared sample (a) Co 2p (Pure Co_3O_4), (b) Co 2p (10Ag/s-CoNi), (c) Ni 2p (Pure $NiFe_2O_4$), (d) Ni 2p (10Ag/s-CoNi), (e) Fe 2p (Pure $NiFe_2O_4$), (f) Fe 2p ((10Ag/s-CoNi), (g) O 1s (10Ag/s-CoNi), and (h) Ag 3d (10Ag/s-CoNi).

A photoluminescence (PL) study of the photocatalytic material reveals insights into photo-induced charge carriers migration, transfer, and separation efficiency. Figure 5.6a shows the PL spectra of as-prepared samples excited by 330 nm radiation. The intensities of all peaks in the PL of the 10Ag/s-CoNi nanocomposite were significantly reduced

compared to Co_3O_4 and $NiFe_2O_4$. The decreased PL intensity was due to the reduced electron-hole recombination rate [186,197]. The latter implies enhanced interfacial charge separation. Figure 5.6b displays the electrochemical impedance spectroscopy (EIS) measurements performed on Co_3O_4, $NiFe_2O_4$, and 10Ag/s-CoNi composite samples. The Nyquist plot of the 10Ag/s-CoNi photocatalyst exhibits a smaller arc radius than Co_3O_4 and $NiFe_2O_4$ samples, pointing to lesser charge transfer resistance and better charge separation [198,199].

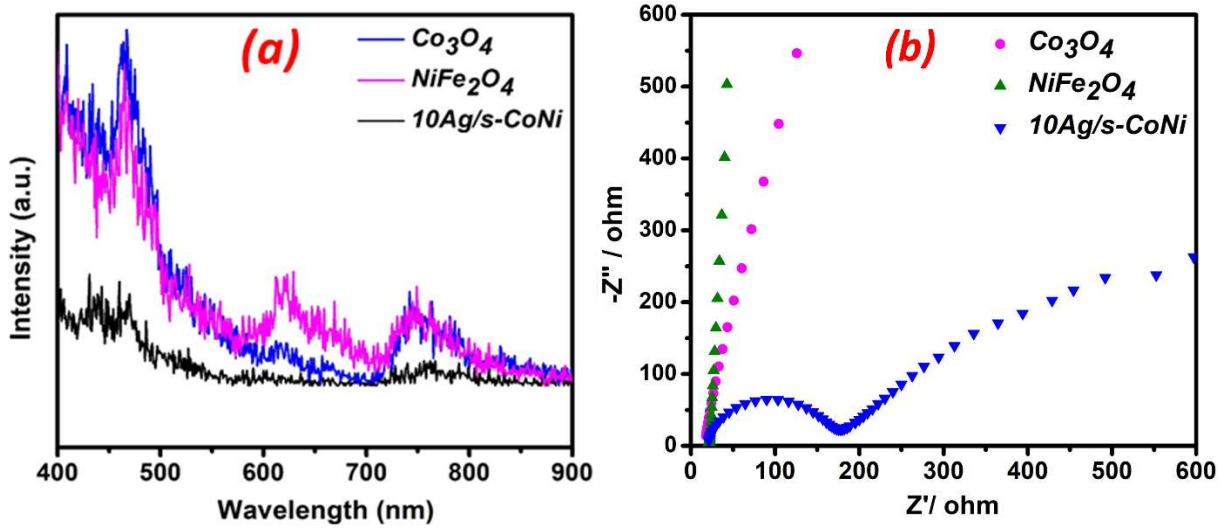

Figure 5.6 (a, b) PL spectra and Nyquist plots of pure $NiFe_2O_4$, Co_3O_4, and 10Ag/s-CoNi composite

Figure 5.7 displays the magnetization curves of the 10Ag/s-CoNi and CoNi composites recorded on a vibrating sample magnetometer (VSM) at room temperature. The x-axis of the graph gives the applied magnetic field (Oe), and the y-axis refers to the magnetization. The saturation magnetizations of 10Ag/s-CoNi and CoNi are 8.34 emu/g and 14.23 emu/g. Both 10Ag/s-CoNi and CoNi are superparamagnetic because there is no hysteresis in their magnetization loop. The inset picture in Figure 5.7 exhibits that the nanoparticles are easily separated when an external magnet is adjacent to the reaction mixture [200].

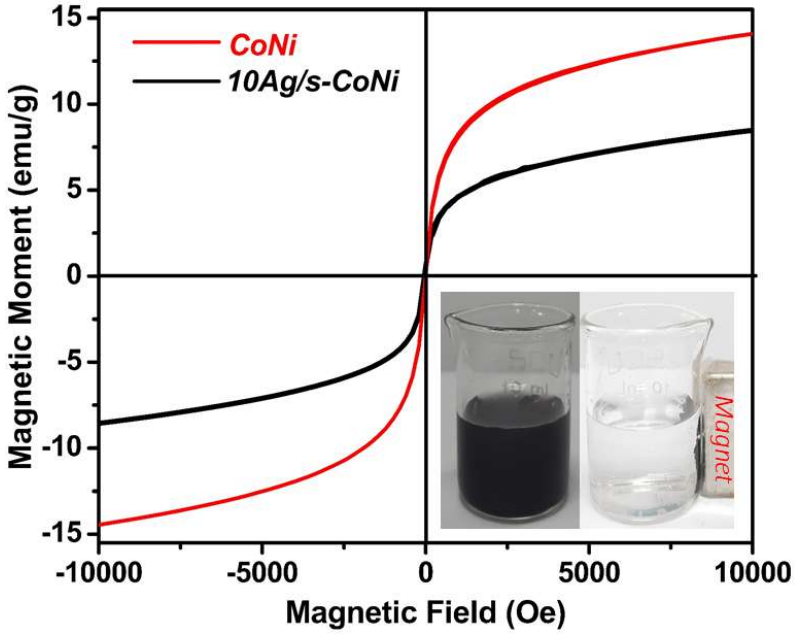

Figure 5.7 Room temperature magnetization curve of CoNi and 10Ag/s-CoNi samples

5.3.1 Molecular dynamics simulation

Figure 5.8a shows a snapshot of the simulated system at the end of a ten-nanosecond run. The oxygen molecules in the system are mostly near the Co_3O_4 surface. A few of them are also on the $NiFe_2O_2$ slab surface. The oxygen molecule density profile along the length of the system describes the situation quantitatively (Figure 5.8b). This density profile graph is a long-time average of the production run. It shows that there is oxygen adsorption on both Co_3O_4 and $NiFe_2O_4$ surfaces. However, the amount of oxygen adsorption on Co_3O_4 is more than double that on the $NiFe_2O_4$ surface.

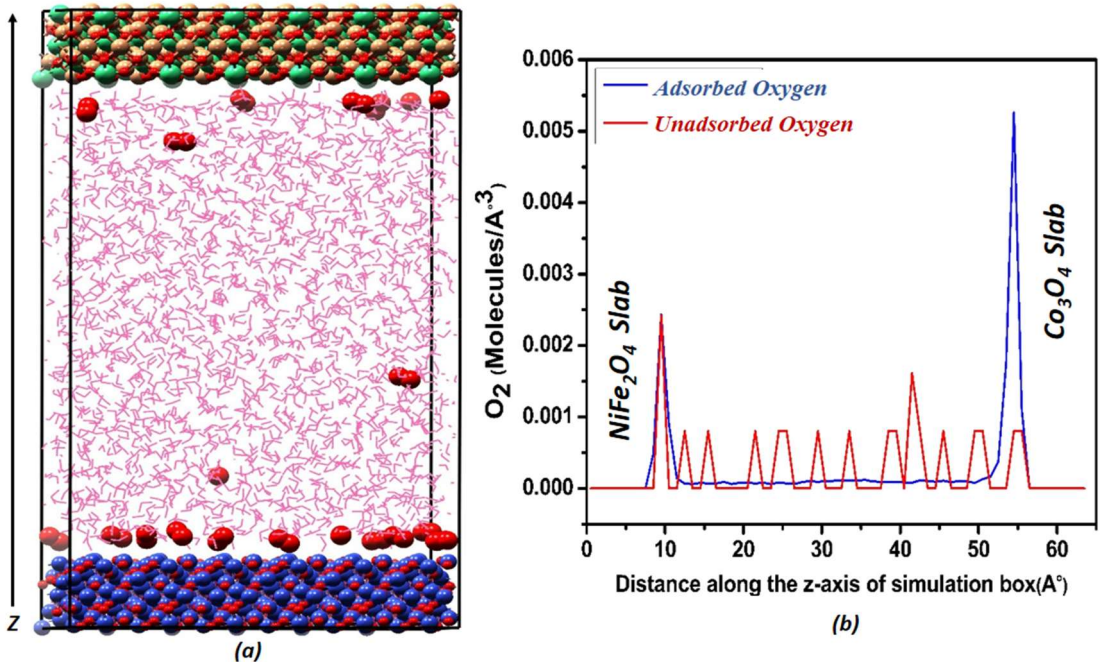

Figure 5.8 (a) A snapshot of oxygen molecules adsorbed on the slab surface after a 10-nanosecond MD simulation and (b) oxygen density profile of oxygen molecules along the z-axis (length) of the simulation cell.

A radial distribution function (RDF) analysis enabled us to understand the interaction among adsorbate, adsorbent, and solvent molecules. The RDF gives us a quantitative knowledge of how atom types constituting the adsorbent surface interact with those making the adsorbate and the solvent molecules. Fig. 5.9a shows the RDFs between oxygen (in the O_2 molecule) and the atom types in the two surfaces (Co_3O_4 and $NiFe_2O_4$). The first RDF peak (blue curve, Co-O) implies that oxygen molecules interact with the Co_3O_4 slab through the surface Co atom types. In contrast, the red and the black curves show that oxygen molecules interact primarily with the Ni atoms in the $NiFe_2O_4$ slab. The blue curve's first peak height is substantially higher than the first peaks of the red and the black curves because of better oxygen adsorption on the Co_3O_4 surface.

Fig. 5.9b gives the RDF between H_2O (solvent) atom types and atoms constituting the two adsorbent surfaces. The dark blue curve [Ni ($NiFe_2O_4$) – O (H_2O)] has the highest

peak among curves in this figure. This curve tells us that $NiFe_2O_4$ interacts with the oxygen of H_2O through the Ni atom type on its surface. The next highest peak is of the green curve and tells us that the Co_3O_4 surface interacts with water molecules through the Co (Co_3O_4) – O (H_2O) interaction.

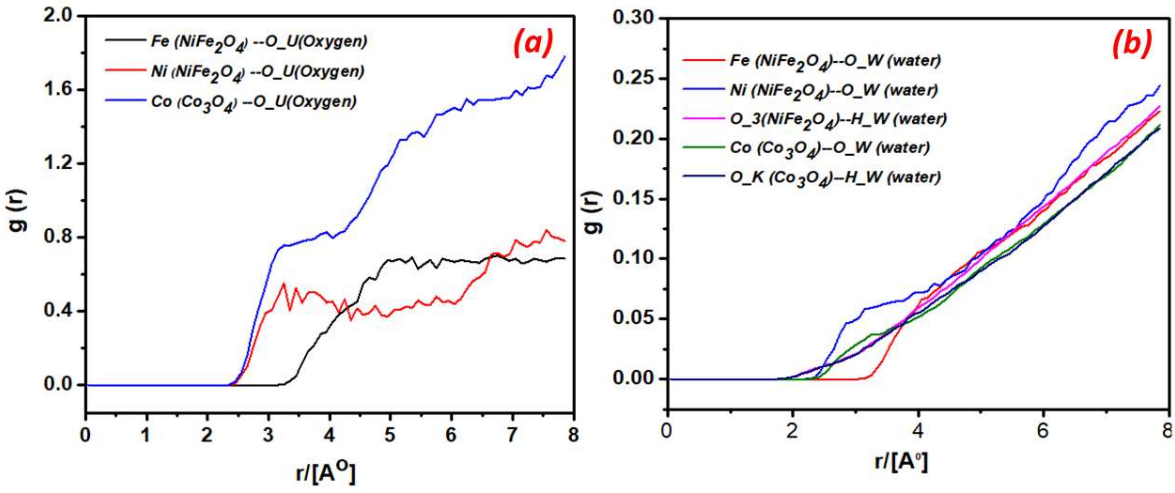

Figure 5.9 (a, b) Radial distribution function g(r) versus distance of interaction r(Å) graph. In the graph, atoms are represented by specific symbols of atom type. Cobalt and oxygen atoms of Co_3O_4 by Co and O_K respectively, Ni and Fe atoms of $NiFe_2O_4$ as Ni and Fe respectively, oxygen of $NiFe_2O_4$ as O_3, hydrogen, and oxygen of water as H_W and O_W respectively, an oxygen atom of O_2 molecule as O_U.

5.3.2 Photocatalytic H_2O_2 production

Photocatalytic H_2O_2 generation was evaluated as per the process discussed in section 5.2.5. Initially, the activity was tested after allowing the reaction mixture to stand for 60 minutes in dark conditions. No H_2O_2 production was noticed in any photocatalytic sample. A significant amount of H_2O_2 was produced after visible light irradiation. Table 5.1 compares the H_2O_2 generation rate over each photocatalyst. Compared to other materials prepared in this investigation, the 10Ag/s-CoNi shows significantly better H_2O_2 generation

activity from pure water (at pH 3 without oxygen purging). The photocatalytic H_2O_2 formation was investigated under different pH conditions, with the optimum activity observed at pH 3. H_2O_2 formation decreased significantly when the pH was increased to 7 (Figure 5.10a).

As mentioned earlier, several control experiments were carried out to ascertain the mechanism of H_2O_2 formation. First, H_2O_2 formation was tested when the experiment was carried out in acetonitrile (instead of water) under continuous O_2 purging. No H_2O_2 formation was observed under these circumstances, confirming the crucial role of water in the process. Photocatalytic H_2O_2 formation from pure water without oxygen purging combined with the results of this control experiment implies water oxidation [201]. Subsequently, the photocatalytic H_2O_2 formation was also tested when the experiment was done in pure water but with continuous oxygen purging. The latter increased H_2O_2 formation by about ~9% than without O_2 purging (Figure 5.10b). The photocatalytic H_2O_2 formation experiment was also carried out with IPA as an electron donor with and without O_2 purging. The addition of 4-vol% IPA in the photocatalytic solution increased H_2O_2 productivity by 15% over pure water. This production was enhanced by another ~8% on carrying out the (4 volume% IPA) experiment under continuous O_2 purging (Figure 5.10b). Fig. 5.10c displays the recyclability plot of photocatalytic H_2O_2 production on 10Ag/s-CoNi, indicating minor changes in the H_2O_2 production activity after five consecutive cycles, confirming the stability of the 10Ag/s-CoNi photocatalyst.

Table 5.1. Photocatalytic H_2O_2 production from pure water (without O_2 purging) over different materials prepared in this research work.

Photocatalyst	**H_2O_2 produced $\mu mol.g^{-1}.h^{-1}$**

Co_3O_4	No activity
$NiFe_2O_4$	No activity
CoNi	121 $\mu molg^{-1}h^{-1}$
10Ag/s-CoNi	1250 $\mu molg^{-1}h^{-1}$
20Ag/s-CoNi	583 $\mu molg^{-1}h^{-1}$

5.3.3 In-situ photo-Fenton degradation of tetracycline

As mentioned earlier, in situ photo-Fenton is an excellent way to utilize generated H_2O_2 in the reaction medium [9,202]. Fig. 5.10d displays the comparison plots of photocatalytic tetracycline degradation (at pH 3) over photocatalysts prepared in this study. In this degradation reaction, the sample 10Ag/s-CoNi exhibited significantly better performance than other samples because of the substantially higher H_2O_2 generation over this photocatalyst (Table 5.1). Figure 5.10e shows that the photocatalytic degradation of tetracycline follows first-order rate kinetics. Tetracycline degradation with IPA in the 10Ag/s-CoNi photocatalyst solution was also investigated. Degradation under these conditions showed ~15% enhancement over the earlier experiment in pure water (Figure 5.10f). This photocatalysis experiment was also implemented in dilute KI and PBQ aqueous solutions. These (KI and PBQ) are scavengers for holes and superoxide reactive species, respectively. The photocatalytic tetracycline degradation slowed down appreciably in the presence of KI (40% of that in pure water). There was little effect of PBQ addition to the reaction medium (Figure 5.10f), showing that superoxide ion ($O_2^{\cdot -}$) is not an active species.

The recyclability of the photocatalyst (10Ag/s-CoNi) was also tested. Fig. 5.10g shows the tetracycline degradation trend for five continuous cycles. Even after five cycles, the photocatalyst showed >82% tetracycline degradation. Hence, the photocatalyst remains stable after repeated cycles. After each cycle, the sample was washed, magnetically

separated, dried, and then used for another cycle. Fig. 5.10h shows the XRD spectrum of the reused 10Ag/s-CoNi photocatalyst. All peaks in the unused 10Ag/s-CoNi powder sample are also visible in the powder pattern of the reused sample, confirming that the nanocomposite remained stable after five consecutive cycles.

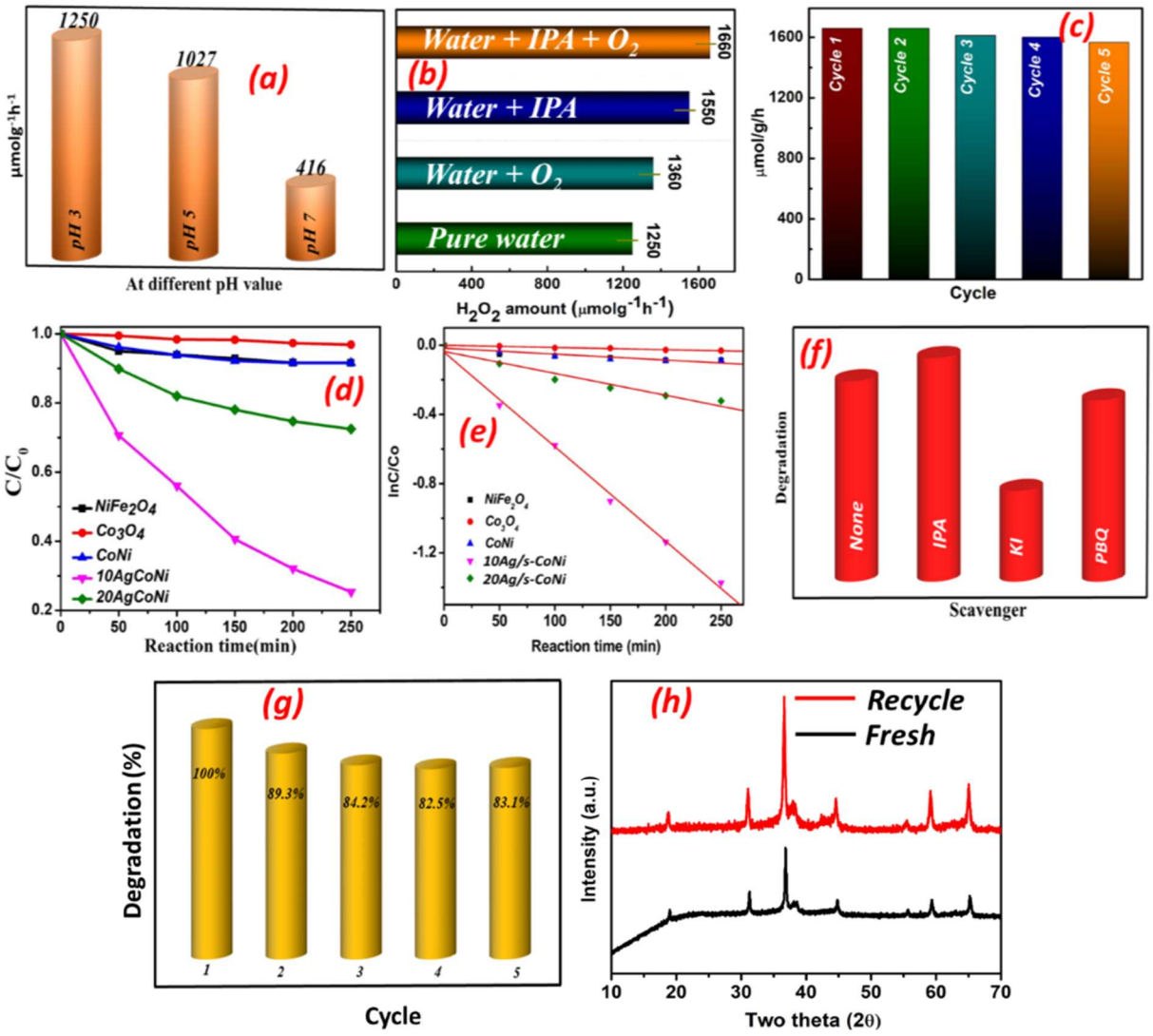

Figure 5.10 (a) H_2O_2 production under different pH conditions. **(b)** H_2O_2 production under various controlled conditions. **(c)** Recyclability plot of H_2O_2 production on 10Ag/s-CoNi photocatalysts. **(d)** Comparison of tetracycline degradation over time using different materials prepared in this study. **(e)** Photocatalytic tetracycline degradation follows first-order kinetics. **(f)** Scavenger studies for tetracycline degradation on the 10Ag/s-CoNi

photocatalyst. **(g)** Bar graph showing tetracycline degradation over the 10Ag/s-CoNi nanocomposite after repeated reuse. **(h)** XRD pattern of the reused sample after five cycles.

5.3.4 Photocatalytic mechanism

This section elucidates the probable photocatalytic reaction mechanism for H_2O_2 production and tetracycline degradation using the experimental and computational evidence detailed above. The visible light irradiation of the photocatalyst (10Ag/s-CoNi) photoexcited both Co_3O_4 and $NiFe_2O_4$ components. The electrons in the $NiFe_2O_4$ CB migrated to the Co_3O_4 CB, while the Co_3O_4 VB holes were transferred to the $NiFe_2O_4$ component VB. The EIS and the PL results show that separating electrons and holes into separate parts of the nanocomposite reduced the probability of charge carrier recombination. Furthermore, the XPS analysis showed charge transfer from both Co_3O_4 and $NiFe_2O_4$ parts to the Ag nanostructures on their surfaces. Thus, Ag nanostructures became electron-rich sites for oxygen reduction.

MD simulation results showed that oxygen adsorption predominantly takes place on the Co_3O_4 surface. The larger size of the Co_3O_4 part of the composite also indicates that more Ag nanostructures would have been deposited on it. Thus, oxygen reduction mainly happens on the Ag nanostructures loaded on this surface. MD simulations also show that $NiFe_2O_4$ components display better affinity toward H_2O than Co_3O_4. The increased concentration of holes on the $NiFe_2O_4$ side means water oxidation primarily occurs on this surface. The schematic in Figure 5.11 summarizes the mechanism proposed above.

The scavenger experiments during the photocatalytic tetracycline degradation also gave vital information about the mechanism. The presence of IPA increased H_2O_2 production and tetracycline degradation, indicating a more effective Fenton-type mechanism. KI (hole scavenger) replaces the oxidation of water molecules on the

photocatalyst VB. Low water oxidation meant lesser oxygen production, lesser H_2O_2 production and severely impeded the photocatalytic degradation of tetracycline. Since superoxide ($\cdot O_2^-$) radicals are not the main reactive species during the photocatalytic reaction, possibly oxygen reduction happens by the two-electron reduction route.

The optimum photocatalytic activity was observed for the 10Ag/s-CoNi photocatalyst, not the 20Ag/s-CoNi sample, because excess Ag loading on the CoNi sample hinders light absorption by constituent Co_3O_4 and $NiFe_2O_4$ components. Superparamagnetic nanocatalysts reduce the cost of catalyst separation and recycling drastically. Overall, the facile magnetic recyclability and efficient and highly economic H_2O_2 production sufficient for organic pollutant degradation imply that the prepared photocatalysts are suitable for industrial use.

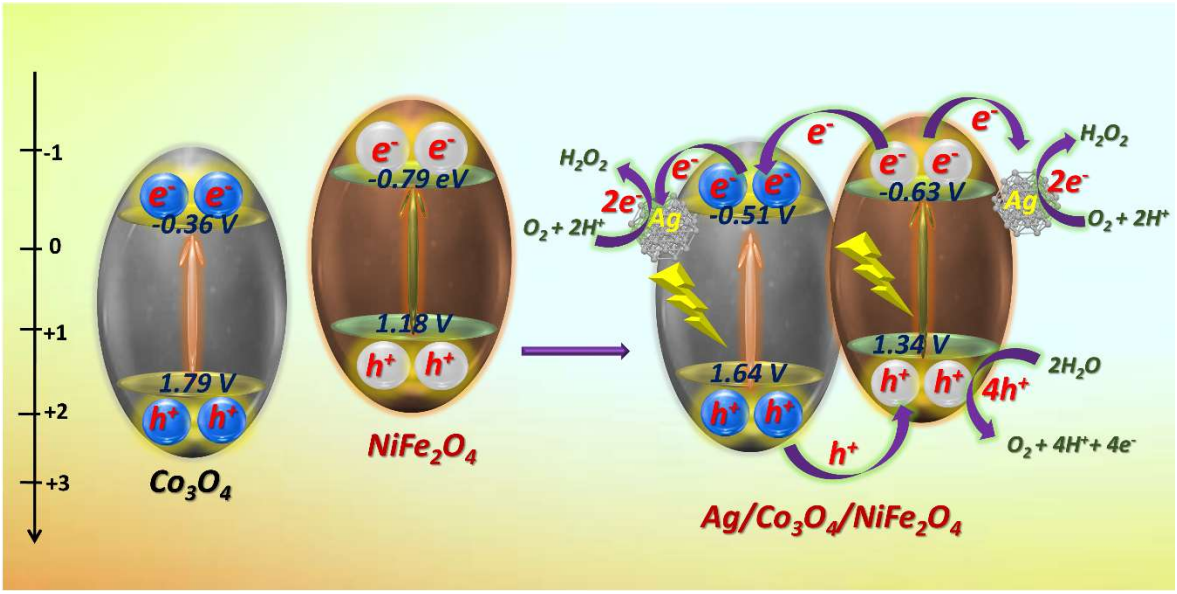

Figure 5.11 Schematic representation of the proposed mechanism on Ag/s-(Co_3O_4/$NiFe_2O_4$) photocatalyst

5.4 Conclusions

An efficient magnetically recyclable photocatalyst for H_2O_2 production from pure water and visible light has been designed and prepared. Co_3O_4 and $NiFe_2O_4$ were selected as the two components for this photocatalyst based on their staggered bandgaps and the relatively higher affinity of Co_3O_4 towards oxygen adsorption. Large-scale molecular dynamics simulation investigations revealed the higher adsorption capacity of oxygen on the Co_3O_4 surface in an aqueous environment. A step-wise precipitation protocol was utilized to prepare the composite. Since Ag nanostructures are well-known for catalyzing oxygen reduction by the 2-electron route, fine Ag nanostructures were deposited on starch-stabilized composite surfaces. Soluble starch stabilized the nanocomposites against aggregation and also made the photocatalyst surface more hydrophilic.

A type II p-n heterojunction photocatalyst was formed. The Ag nanostructures on the composite surface acted as electron oxygen reduction centers while the holes were concentrated on the $NiFe_2O_4$ side. The 10Ag/s-CoNi exhibited the best photocatalytic H_2O_2 production activity in pure water (without any oxygen purging). The photocatalyst also degradation tetracycline efficiently. Excess Ag precipitation on the CoNi composite lowered its photocatalytic activity. Adding isopropyl alcohol (the electron donor) to water further increased the H_2O_2 formation activity. It also increased the photocatalytic tetracycline degradation rate. Economic magnetic recyclability and production of H_2O_2 from pure water and visible light make this photocatalyst industrially viable.